UCLA

UCLA Previously Published Works

Title

Determining the three-dimensional atomic structure of an amorphous solid

Permalink

https://escholarship.org/uc/item/9k11s6nr

Journal

Nature, 592(7852)

ISSN

0028-0836

Authors

Yang, Yao

Zhou, Jihan

Zhu, Fan

et al.

Publication Date

2021-04-01

DOI

10.1038/s41586-021-03354-0

Copyright Information

Peer reviewed

Determining the three-dimensional atomic structure of an amorphous solid

Yao Yang[1*], Jihan Zhou[1*], Fan Zhu[1*], Yakun Yuan[1*], Dillan J. Chang[1], Dennis S. Kim[1], Minh Pham[2], Arjun Rana[1], Xuezeng Tian[1], Yonggang Yao[3], Stanley J. Osher[2], Andreas K. Schmid[4], Liangbing Hu[3], Peter Ercius[4] & Jianwei Miao[1]

[1]Department of Physics & Astronomy, STROBE NSF Science & Technology Center and California NanoSystems Institute, University of California, Los Angeles, CA 90095, USA.

[2]Department of Mathematics, University of California, Los Angeles, CA 90095, USA.

[3]Department of Materials Science and Engineering, University of Maryland, College Park, Maryland, 20742, USA. [4]National Center for Electron Microscopy, Molecular Foundry, Lawrence Berkeley National Laboratory, Berkeley, CA 94720, USA.

[*]These authors contributed equally to this work.

Amorphous solids such as glass are ubiquitous in our daily life and have found broad applications ranging from window glass and solar cells to telecommunications and transformer cores[1,2]. However, due to the lack of long-range order, the three-dimensional (3D) atomic structure of amorphous solids has thus far defied any direct experimental determination without model fitting[3-13]. Here, using a multi-component glass-forming alloy as a proof-of-principle, we advance atomic electron tomography to determine the 3D atomic positions in an amorphous solid for the first time. We quantitatively characterize the short-range order (SRO) and medium-range order (MRO) of the 3D atomic arrangement. We find that although the 3D atomic packing of the SRO is geometrically disordered, some SROs connect with each other to form crystal-like superclusters and give rise to the MRO. We identify four crystal-like MROs – face-centred cubic, hexagonal close-packed, body-centered

cubic and simple cubic – coexisting in the amorphous sample. These observations provide direct experimental evidence to support the general framework of the efficient cluster packing model[8,10-12,20]. Looking forward, we anticipate this experiment will open the door to determining the 3D atomic coordinates of various amorphous solids, whose impact on non-crystalline solids may be comparable to the first 3D crystal structure solved by x-ray crystallography over a century ago[14].

Since the first discovery in 1960[15], metallic glasses have been actively studied for fundamental interest and practical applications[7-12,16-20]. However, due to their disordered structure, the 3D atomic arrangement of metallic glasses cannot be determined by crystallography[21]. Over the years, a number of experimental and computational methods have been used to study the metallic glass structure, such as x-ray/neutron diffraction[22,23], x-ray absorption fine structure[9], high-resolution transmission electron microscopy[24], fluctuation electron microscopy[25], angstrom- and nano-beam electron diffraction[13,26,27], nuclear magnetic resonance[28], density functional theory[29], molecular dynamics simulations[30-33] and reverse Monte Carlo modelling[9,25]. Despite all these developments, however, there was no experimental method available to directly determine all the 3D atomic positions in metallic glass samples. One experimental method that can in principle solve this long-standing problem is atomic electron tomography (AET)[34,35]. AET combines high-resolution tomographic tilt series with advanced iterative algorithms to resolve the 3D atomic structure of materials without assuming crystallinity, which has been applied to image grain boundaries, anti-phase boundaries, stacking faults, dislocations, point defects, chemical order/disorder, atomic-scale ripples, bond distortion and strain tensors with unprecedented 3D detail[36-41]. More recently, 4D (3D + time) AET has been developed to observe crystal nucleation at atomic resolution, showing that early

49   stage nucleation results are inconsistent with classical nucleation theory[42]. Here, we use

50   an amorphous sample of glass-forming alloy as a model and advance AET to determine

51   its 3D atomic positions with a precision of 21 picometers.

3D atomic positions in a glass-forming alloy

53   The samples were synthesized by a carbothermal shock technique with a high cooling

54   rate (Extended Data Fig. 1a, Supplementary video 1 and Methods), which was used to

55   create high entropy alloy nanoparticles with multi-metal components[43]. The energy-

56   dispersive X-ray spectroscopy data show the nanoparticles are composed of eight

57   elements: Co, Ni, Ru, Rh, Pd, Ag, Ir and Pt (Extended Data Fig. 1b-k). Tomographic tilt

58   series were acquired from seven nanoparticles using a scanning transmission electron

59   microscope with an annular dark-field detector (Extended Data Table 1). While most of

60   the nanoparticles are crystalline or polycrystalline, particles 1 and 2 have disordered

61   structure (Extended Data Fig. 2). In this study, we focus on the most disordered

62   nanoparticle (particle 1), from which a tilt series of 55 images was acquired (Fig. 1a and

63   Extended Data Fig. 3). Although some crystalline features are present in several images,

64   the 2D power spectra calculated from the images show the amorphous halo.

65   After pre-processing and image denoising, the tilt series was reconstructed and

66   the 3D atomic positions were traced and classified (Fig. 1c, d, Supplementary Video 2

67   and Methods). Since the image contrast in the 3D reconstruction depends on the atomic

68   number[40-42], presently AET is only sensitive enough to classify the eight elements into

69   three different types: Co and Ni as type 1, Ru, Rh, Pd and Ag as type 2, and Ir and Pt as

70   type 3. After atom classification, we obtained the 3D atomic model of the nanoparticle,

71   consisting of 8322, 6896 and 3138 atoms for type 1, 2 and 3, respectively. To verify the

72   reconstruction, atom tracing and classification procedure, we calculated 55 images from

the experimental atomic model using multislice simulations (Methods). Extended Data Fig. 4c and d shows the consistency between the experimental and calculated images. We then applied the reconstruction, atom tracing and classification procedure to obtain a new 3D atomic model from the 55 multislice images. By comparing the two models, we estimated that 97.37% of atoms were correctly identified with a 3D precision of 21 pm (Methods and Extended Data Fig. 4e).

Figure 1e and Supplementary video 3 show the experimental 3D atomic model of the nanoparticle with type 1, 2 and 3 atoms in green, blue and red, respectively. To quantitatively characterize the atomic structure, we employed the local bond orientational order (BOO) parameters to distinguish between the disordered, face-centred cubic (fcc), hexagonal close-packed (hcp) and body-centered cubic (bcc) structures (Methods). Figure 1f shows the local BOO parameters of all the atoms in the nanoparticle, indicating the majority of atoms severely deviate from the fcc, hcp and bcc crystal structures. For a comparison, the local BOO parameters of all the seven nanoparticles are shown in Extended Data Fig. 2h-n. To separate crystal nuclei from the amorphous structure, we used the normalized BOO parameter to identify the crystal nuclei (Methods). By choosing the criterion of the normalized BOO parameter ≥ 0.5 (Extended Data Fig. 2o), we identified 15.46% of the total atoms forming crystal nuclei in the nanoparticle (Extended Data Fig5a), which contribute to the crystalline features observed in several images (Extended Data Fig. 3). The characteristic width of the crystalline-amorphous interface was determined to be 3.69 Å in the nanoparticle (Methods), indicating that the crystal nuclei have a minimal effect on the structural disorder beyond a few angstroms. In the following sections, we focus on the analysis of the disordered atoms with the normalized BOO parameter < 0.5.

97   Figure 1g shows the pair distribution function (PDF) of the amorphous structure

98   of the 3D atomic model (Methods), where the weak second-peak splitting is consistent

99   with previous observation in high entropy bulk metallic glasses[44]. The ratios of the

100   second, third, fourth and fifth to the first peak position are 1.74, 1.99, 2.64 and 3.51,

101   respectively, which are in good agreement with those of metallic glasses[45,46]. The partial

102   PDFs between type 1, 2 and 3 atoms are shown in Fig. 1h. By fitting a Gaussian to the

103   first peaks in the partial PDFs, we determined the type 11, 12, 13, 22, 23 and 33 bond

104   lengths to be 2.59, 2.71, 2.78, 2.72, 2.75 and 2.9 Å, respectively. In particular, the partial

105   PDF for the type 33 pairs (the yellow curve) exhibits a unique feature with the second

106   peak higher than the first peak, indicating that the majority of type 3 atoms are distributed

107   beyond the SRO.

108   **The short-range order**

109   To determine the SRO in the glass-forming nanoparticle, we used the Voronoi tessellation

110   to characterize the local atomic arrangement[6]. This method identifies the nearest

111   neighbour atoms around each central atom to form a Voronoi polyhedron, which is

112   designated by a Voronoi index $<n_3, n_4, n_5, n_6>$ with n_i denoting the number of i-edged

113   faces. Figure 2a shows the ten most abundant Voronoi polyhedra in the nanoparticle with

114   a fraction ranging from 5.02% to 1.72%, most of which are geometrically disordered and

115   commonly observed in model metallic glasses[11] such as $<0,4,4,3>$, $<0,3,6,3>$, $<0,4,4,2>$

116   and $<0,3,6,2>$ (Fig. 2b). To examine the effect of the precision of AET on the Voronoi

117   analysis, we added the experimental error (Extended Data Fig. 4e) to a $Cu_{65}Zr_{35}$ metallic

118   glass model obtained from molecular dynamics simulations. By comparing the Voronoi

119   polyhedra with and without the error, we found that the precision of AET has only a small

120   effect on the Voronoi tessellation (Methods). This result suggests that the small fractions

121 of the Voronoi polyhedra in the glass-forming nanoparticle are mainly due to its poor

122 glass forming ability[11,18].

123   Figure 2c shows the local symmetry distribution of all the faces of the Voronoi

124 polyhedra. The 3-, 4-, 5- and 6-edged faces account for 3.27%, 29.14%, 43.91% and

125 23.67%, respectively, revealing that 5-edged faces are most abundant in the SRO. But

126 only 7.03% of all the Voronoi polyhedra are distorted icosahedra, including Voronoi

127 indices <0,0,12,0>, <0,1,10,2>, <0,2,8,2> and <0,2,8,1>. This observation indicates that

128 most 5-edged faces do not form distorted icosahedra in this glass-forming nanoparticle.

129 From the Voronoi tessellation, we also calculated the distribution of the coordination

130 number (CN) (Fig. 2d and Methods), where the average CNs of types 1, 2 and 3 atoms

131 are 11.97, 12.02 and 12.41, respectively. Based on the partial CNs (Extended Data Fig.

132 5b), we quantified the chemical SRO using the Warren–Cowley parameters (Methods),

133 indicating that the type 11 and 23 bonds are favoured, but the type 12 and 33 bonds are

134 unfavoured. These results are consistent with the observations of the shortening of the

135 type 11 and 23 bonds and the lengthening of the type 12 and 33 bonds (Methods).

136 **The medium-range order**

137 While the MRO in metallic glasses is broadly defined as the nanometre-scale structural

138 organization beyond the SRO[8-13,20,25,26,31], in this work we focused on the investigation of

139 the MRO in the framework of the efficient cluster packing model[8,12]. This model

140 hypothesizes that solute atoms are surrounded by randomly-positioned solvent atoms to

141 form solute-centred clusters, which are densely packed to constitute crystal-like MROs

142 in metallic glasses. To quantitatively test this model with experimental data, we analysed

143 the partial PDF of type 33 atom pairs (Fig. 1h, the yellow curve) and observed that the

144 highest peak is at 4.77 Å and 1.49 times higher than the nearest neighbour peak. We found

that 85.47% of type 3 atoms are distributed in the second coordination shell (Extended Data Fig. 5c and Methods), which is between the first (3.86 Å) and the second minimum (6.08 Å) of the PDF curve (Fig. 1g). These type 3 atoms act as solute atoms and are surrounded mainly by type 1 and 2 solvent atoms to form solute-centred clusters. Extended Data Fig. 5d shows the ten most abundant Voronoi polyhedra of these clusters. The solute-centred clusters connect with each other by sharing one (a vertex), two (an edge) and three atoms (a face) as well as protrude into each other by sharing four and five atoms (Fig. 3a-e). Figure 3f shows the statistical distribution of the number of the solute-centred cluster pairs, which share from one to five atoms.

To locate the MRO in the glass-forming nanoparticle, we implemented a breadth-first search algorithm to look for the fcc-, hcp-, bcc-, simple cubic (sc-) and icosahedral-like structures of the solute centres (Methods). This algorithm globally searches for the MRO with a maximum number of solute centres. Each MRO is defined to have five or more solute centres with each solute centre falling within a 0.75 Å radius to the fcc, hcp, bcc, sc lattice or icosahedral vertices. We found that four types of MROs (fcc-, hcp-, bcc- and sc-like) coexist in the sample (Methods). Although we did not observe icosahedral-like MROs in this sample, our work does not rule out its existence in other metallic glasses[9]. Figure 3g shows the histogram of the four types of MROs as a function of the size, where the inset illustrates the fraction of the solute centre atoms in the four types of MROs. Figure 3h and Supplementary Video 4 show the 3D distribution of MROs with each having eight solute centres or more. To verify our analysis, we also searched for MROs with a 1 Å and 0.5 Å radius cut-off and observed the coexistence of the four types of MROs with different cut-off radii (Extended Data Figs. 6 and 7).

168   Next, we quantitatively characterized MROs with a 0.75 Å radius cut-off. Figure

169   4a and b show the length and volume distribution of the MROs in the glass-forming

170   nanoparticle. The average length of the fcc-, hcp-, bcc- and sc-like MROs was measured

171   to be 2.27 ± 0.50, 2.40 ± 0.42, 2.07 ± 0.38, 2.11 ± 0.48 nm, respectively, with the

172   corresponding average volume of 1.80 ± 0.64, 1.96 ± 0.53, 1.63 ± 0.46 and 1.96 ± 0.74

173   nm^3. Figure 5a, c, e and g show four representative fcc-, hcp-, bcc- and sc-like MROs, in

174   which the individual solute-centred clusters are randomly oriented. To better visualize

175   these MROs, the solute centres are orientated along the fcc, hcp, bcc and sc zone axes

176   (Fig. 5b, d, f and h), showing that the 3D shapes of the MROs are anisotropic. We

177   calculated the partial PDFs of all the fcc-, hcp-, bcc- and sc-like solute centres in the glass-

178   forming nanoparticle and their corresponding maximum peak positions are at 4.62, 4.77,

179   4.82 and 3.88 Å, respectively (Fig. 4c). These peak positions represent the average nearest

180   neighbour distances of the solute centres in the four crystal-like MROs and the broadened

181   peaks signify the severe deviation from the crystal lattices. Compared with the other three

182   partial PDFs, the partial PDF of the sc-like MROs has two peaks and the ratio of the

183   second to the first peak position is about $\sqrt{2}$ (Fig. 4c, the purple curve), which

184   corresponds to the ratio of the diagonal to the side length of a square. The shorter nearest

185   neighbour distance of the sc-like MROs compared to the other three crystal-like MROs

186   indicates that the sc-like solute-centred clusters are more closely connected with their

187   neighbours. Figure 4d shows the distribution of sharing one, two, three, four and five

188   atoms between neighbouring solute-centred clusters for the four types of MROs,

189   confirming that the solute-centred clusters in the sc-like MROs tend to share more atoms

190   with their neighbours than those in other types of MROs.

191   Our quantitative analysis of the SRO and MRO in a multi-component glass-

192   forming nanoparticle provides direct experimental evidence to support the general

193   framework of the efficient cluster packing model[8,10-12,20], that is, solute-centred clusters

194   are densely packed in some parts of the sample to form crystal-like MROs. We observed

195   the chemical SRO, the bond shortening and lengthening, and the coexistence of fcc-, hcp-

196   , bcc- and sc-like MROs in the glass-forming nanoparticle. By quantifying their length,

197   volume and 3D structure, we found that the MROs not only has a large variation in length

198   and volume, but also severely deviates from the crystal lattices (Fig. 4c). As the size of

199   the MROs is comparable to that of shear transformation zones in metallic glasses[11,20,47,48],

200   we expect that AET could also be applied to determine the 3D atomic structures related

201   to shear transformation zones and link the structure and properties of metallic glasses[11].

202   **Outlook**

203   Over the last century, crystallography has been broadly applied to determine the 3D

204   atomic structure of crystalline samples[21]. The quantitative 3D structural information has

205   been fundamental to the development of many scientific fields. However, for amorphous

206   solids, their 3D structure has been primarily inferred from experimental data, where either

207   the average statistical structural information can be obtained or model fitting is required

208   to analyse the local atomic order[8-13]. These qualitative approaches have hindered our

209   fundamental understanding of the 3D structure of amorphous solids and related

210   phenomena such as the crystal-amorphous phase transition and the glass transition[11,49,50].

211   Here, we demonstrate the ability to directly determine the 3D atomic structure of an

212   amorphous solid using AET, which enables us to quantitatively analyse the SRO and

213   MRO at the single-atom level. Although we focus on a multi-component glass-forming

214   nanoparticle in this study, this method is generally applicable to different sample

215 geometries such as thin films and extended objects (Extended Data Figs. 8 and 9,

216 Methods). Thus, we expect that this work could open a new era in determining the 3D

217 structure of a wide range of amorphous solids.

218 **References**

219 1. Zallen, R. *The Physics of Amorphous Solids* (Wiley, 1998).

220 2. Elliott, S. R. *Physics of Amorphous Materials* (Harlow, Essex, England: Longman

221 Scientific & Technical, 1990).

222 3. Zachariasen, W. H. The atomic arrangement in glass. *J. Am. Chem. Soc.* **54**, 3841-3851

223 (1932).

224 4. Bernal, J. D. & Mason, J. Packing of spheres: co-ordination of randomly packed

225 spheres. *Nature* **188**, 910-911 (1960).

226 5. Scott, G. D. Packing of equal spheres. *Nature* **188**, 908-909 (1960).

227 6. Finney, J. L. Random packings and structure of simple liquids. 1. Geometry of random

228 close packing. *Proc. Roy Soc. Lond. Ser. A - Math. Phys. Sci.* **319**,479-493 (1970).

229 7. Nelson, D. R. & Spaepen, F. Polytetrahedral order in condensed matter. *Solid State

230 Phys.* **42**, 1-90 (1989).

231 8. Miracle, D. B. A structural model for metallic glasses. *Nat. Mater.* **3**, 697-702 (2004).

232 9. Sheng, H. W., Luo, W. K., Alamgir, F. M., Bai, J. M. & Ma, E. Atomic packing and

233 short-to-medium-range order in metallic glasses. *Nature* **439**, 419-425 (2006).

234 10. Miracle, D. B., Egami, T., Flores, K. M. & Kelton, K. F. Structural aspects of metallic

235 glasses. *MRS Bull.* **32**, 629-634 (2007).

236 11. Cheng, Y. Q. & Ma, E. Atomic-level structure and structure-property relationship in

237 metallic glasses. *Prog. Mater. Sci.* **56**, 379-473 (2011).

238 12. Miracle, D. B. A Physical Model for Metallic Glass Structures: An Introduction and

239 Update. *JOM* **64**, 846–855(2012).

240   13. Hirata, A.et al. Geometric frustration of icosahedron in metallic glasses. *Science* **341,**
241   376-379 (2013).

242   14. Bragg, W. L. The structure of some crystals as indicated by their diffraction of X-rays.
243   *Proc. R. Soc. London Ser*. A **89**, 248-277 (1913).

244   15. Klement Jun, W., Willens, R. H. & Duwez, P. Non-crystalline structure in solidified
245   gold–silicon alloys. *Nature* **187**, 869-870 (1960).

246   16. Greer, A. L. Metallic glasses. *Science* **267**, 1947-1953 (1995).

247   17. Peker, A. & Johnson, W. L. A highly processable metallic glass: $Zr_{41.2}Ti_{13.8}Cu_{12.5}Ni_{10.}$
248         $_{0}Be_{22.5}$. *Appl. Phys. Lett*. **63**, 2342-2344 (1993).

249   18. Inoue, A. Stabilization of metallic supercooled liquid and bulk amorphous alloys. *Acta*
250   *Mater.* **48**, 279-306 (2000).

251   19. Wang, W. H., Dong, C. & Shek. C. H. Bulk metallic glasses. *Mater. Sci. Eng.: R: Rep.*
252   **44**, 45-89 (2004).

253   20. Chen, M.W. A brief overview of bulk metallic glasses. *NPG Asia Mater.* **3**, 82-90
254   (2011).

255   21. Crystallography at 100. *Science* **343**, 1091-1116 (2014).

256   22. Egami, T. & Billinge, S. J. L. *Underneath the Bragg Peaks: Structural Analysis of*
257   *Complex Materials.* (Pergamon Materials Series, v.7, 2003).

258   23. Kelton, K. F. et al. First X-ray scattering studies on electrostatically levitated metallic
259   liquids: demonstrated influence of local icosahedral order on the nucleation barrier.
260   *Phys. Rev. Lett.* **90**, 195504 (2003).

261   24. Zhong, L., Wang, J., Sheng, H., Zhang, Z. & Mao, S. X. Formation of monatomic
262   metallic glasses through ultrafast liquid quenching. *Nature* **512**, 177-180 (2014).

263   25. Hwang, J. et al. Nanoscale structure and structural relaxation in $Zr_{50}Cu_{45}A_{l5}$ bulk
264   metallic glass. *Phys. Rev. Lett.* **108**, 195505 (2012).

265   26. Hirata, A. et al. Direct observation of local atomic order in a metallic glass. *Nat. Mater.*
266   **10**, 28-33 (2011).

267   27. Pekin, T.C. et al. Direct measurement of nanostructural change during in situ

268   deformation of a bulk metallic glass. *Nat. Commun.* **10**, 2445 (2019).

269   28. Tang, X. P., Geyer, U., Busch, R., Johnson, W. L. & Wu, Y. Diffusion mechanisms in

270   metallic supercooled liquids and glasses. *Nature* **402**, 160-162 (1999).

271   29. Sachdev, S. & Nelson, D. R. Order in metallic glasses and icosahedral crystals. *Phys.*

272   *Rev. B* **32**, 4592-4606 (1985).

273   30. Tang, C., & Harrowell, P. Anomalously slow crystal growth of the glass-forming alloy

274   CuZr. *Nat. Mater.* **12**, 507-511 (2013).

275   31. Cheng, Y. Q., Ma, E. & Sheng, H. W. Atomic level structure in multicomponent bulk

276   metallic glass. *Phys. Rev. Lett.* **102**, 245501 (2009).

277   32. Hu, Y. C., Li, F. X., Li, M. Z., Bai, H. Y. & Wang, W. H. Five-fold symmetry as

278   indicator of dynamic arrest in metallic glass-forming liquids. *Nat. Commun.* **6**, 8310

279   (2015).

280   33. Ding, J. & Ma, E. Computational modeling sheds light on structural evolution in

281   metallic glasses and supercooled liquids. *Npj Comput. Mater*. **3**, 9 (2017).

282   34. Scott, M. C. et al. Electron tomography at 2.4-angstrom resolution. *Nature* **483**, 444-

283   447 (2012).

284   35. Miao, J., Ercius, P. & Billinge, S. J. L. Atomic electron tomography: 3D structures

285   without crystals. *Science* **353**, aaf2157 (2016).

286   36. Chen, C.-C. et al. Three-dimensional imaging of dislocations in a nanoparticle at atomic

287   resolution. *Nature* **496**, 74-77 (2013).

288   37. Goris, B. et al. Three-Dimensional Elemental Mapping at the Atomic Scale in

289   Bimetallic Nanocrystals. *Nano Lett.* **13**, 4236-4241 (2013).

290   38. Xu, R. et al. Three-dimensional coordinates of individual atoms in materials revealed by

291   electron tomography. *Nat. Mater.* **14**, 1099-1103 (2015).

39. Haberfehlner, G. et al. Formation of bimetallic clusters in superfluid helium nanodroplets analysed by atomic resolution electron tomography. *Nat. Commun.* **6**, 8779 (2015).

40. Yang, Y. et al. Deciphering chemical order/disorder and material properties at the single-atom level. *Nature* **542**, 75-79 (2017).

41. Tian, X. et al. Correlating the three-dimensional atomic defects and electronic properties of two-dimensional transition metal dichalcogenides. *Nat. Mater.* **19**, 867–873 (2020).

42. Zhou, J. et al. Observing crystal nucleation in four dimensions using atomic electron tomography. *Nature* **570**, 500-503 (2019).

43. Yao, Y. et al. Carbothermal shock synthesis of high-entropy-alloy nanoparticles. *Science* **359**, 1489-1494 (2018).

44. Kim, J. Y. et al. Utilization of high entropy alloy characteristics in Er-Gd-Y-Al-Co high entropy bulk metallic glass. *Acta Mater.* **155**, 350-361 (2018).

45. Liu, X. J. et al. Metallic liquids and glasses: atomic order and global packing. *Phys. Rev. Lett.* **105**, 155501 (2010).

46. Wu, Z. W., Li, M. Z., Wang, W. H. Liu, K.X. Hidden topological order and its correlation with glass-forming ability in metallic glasses. *Nat. Commun*. **6**, 6035 (2015).

47. Spaepen, F. A microscopic mechanism for steady state inhomogeneous flow in metallic glasses. *Acta Metall.* **25**, 407-415 (1977).

48. Argon A. S. Plastic-deformation in metallic glasses. *Acta Metall.* **27**, 47–58 (1979).

49. Johnson, W. L. Thermodynamic and kinetic aspects of the crystal to glass transformation in metallic materials. *Prog. Mater. Sci.* **30**, 81-134 (1986).

50. Debenedetti, P. G. & Stillinger, F. H. Supercooled liquids and the glass transition. *Nature* **410**, 259-267 (2001).

Figures and figure legends
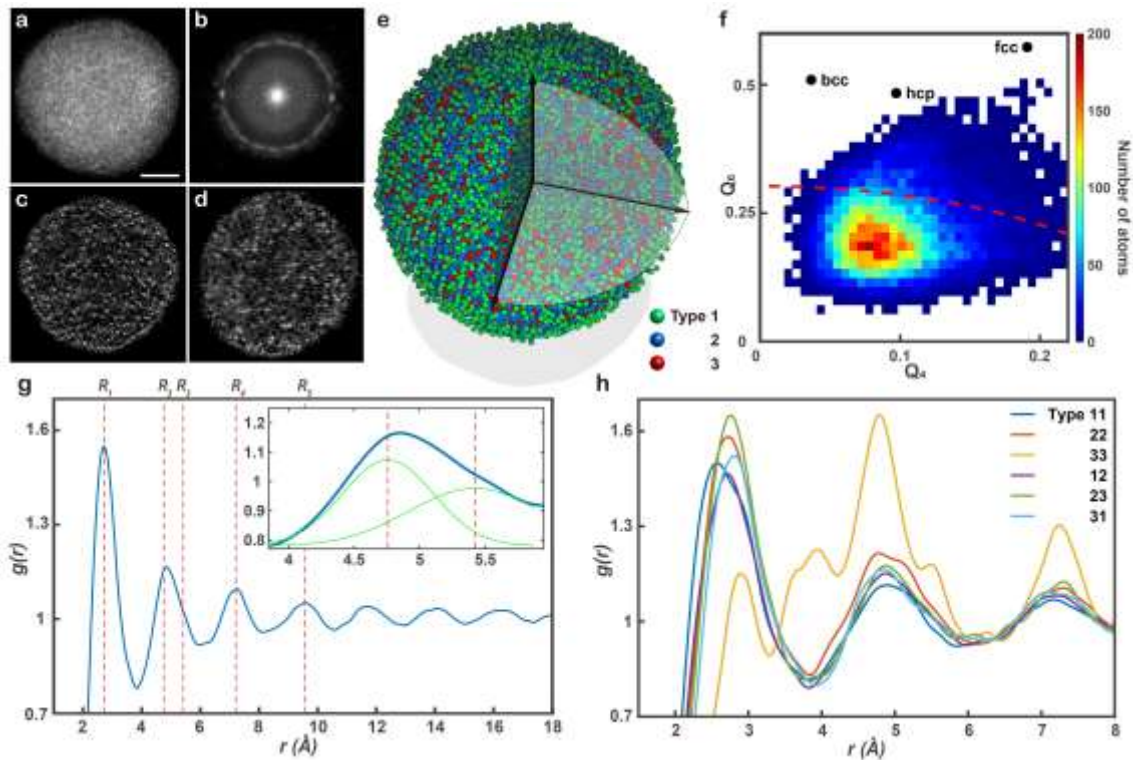
**Figure 1 | Determining the 3D atomic structure of a multi-component glass-forming nanoparticle with AET**. **a,** A representative experimental image, where some crystalline features are visible. Scale bar, 2 nm. **b**, Average 2D power spectrum of 55 experimental images (Extended Data Fig. 3), showing the amorphous halo. **c**, **d**, Two 2.4-Å-thick slices of the 3D reconstruction in the *xy*- and *yz*-plane, respectively, where the majority of type 3 atoms (bright dots) are distributed in the second coordination shell. **e**, Experimental 3D atomic model of the glass-forming nanoparticle. **f**, The local BOO parameters of all the atoms in the nanoparticle. Based on the criterion of the normalized BOO parameter < 0.5 (the dashed red curve), 84.54% of the total atoms are disordered. **g**, The PDF of the disordered atoms with the first, second, third, fourth and fifth peak positions (R_1, R_2, R_3, R_4 and R_5) at 2.73, 4.76, 5.42, 7.22 and 9.57 Å, respectively. The inset shows the second-peak splitting with a Gaussian fit. **h**, The partial PDFs between type 1, 2 and 3 atoms, consisting of 6 pairs - types 11, 12, 13, 22, 23 and 33. The partial PDF for the type 33

332   pairs (the yellow curve) shows a unique feature with a higher second peak than the first

333   peak.
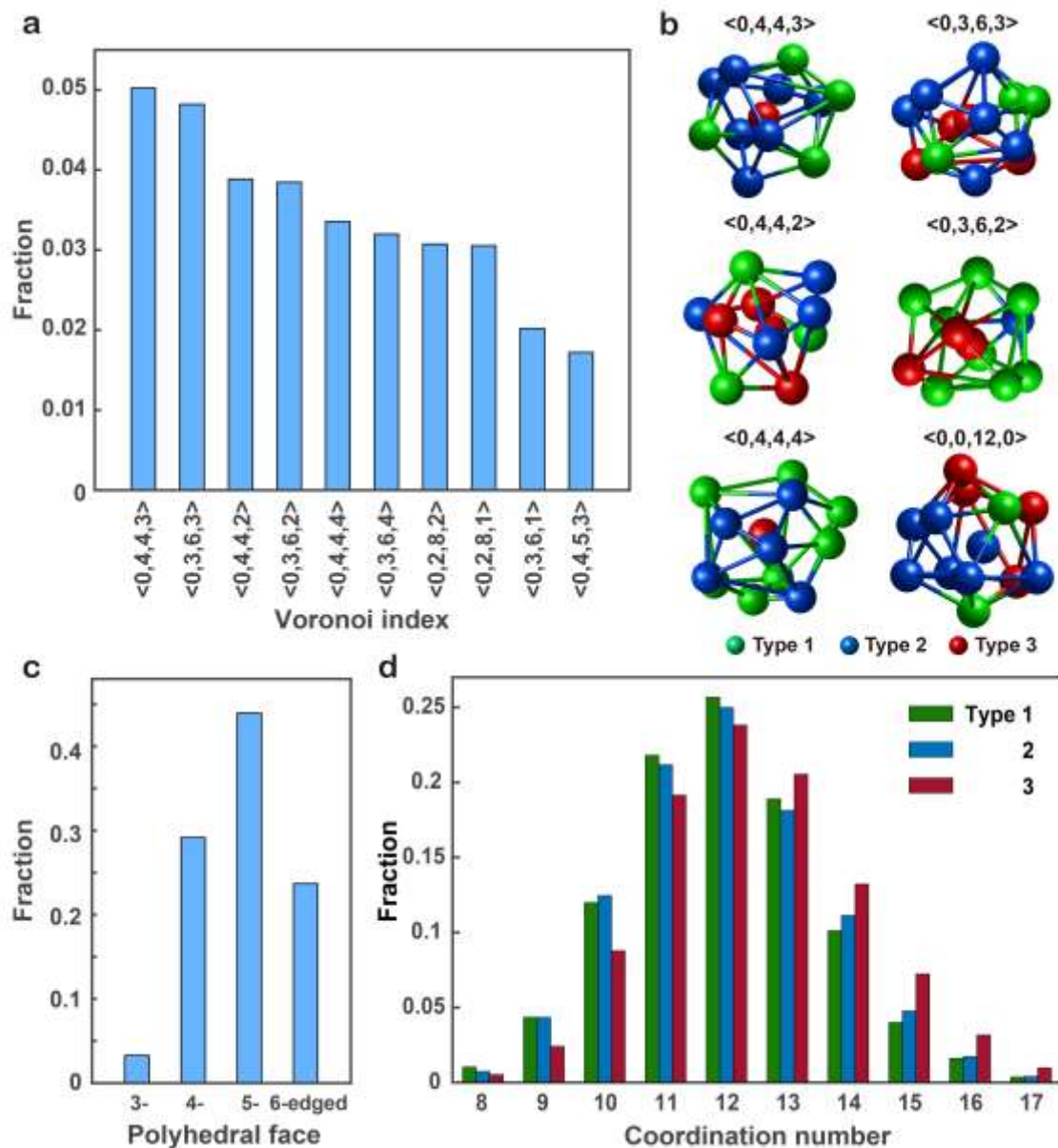
334

335   **Figure 2 | The short-range order of the glass-forming nanoparticle**. **a**, Ten most

336   abundant Voronoi polyhedra in the nanoparticle. **b**, Six representative Voronoi polyhedra,

337   where <0,4,4,3>, <0,3,6,3>, <0,4,4,2> and <0,3,6,2> are the four highest fraction Voronoi

338   indices, <0,4,4,4> shows a severely distorted polyhedron, and <0,0,12,0> represents an

339   icosahedron. **c**, The 3-, 4-, 5- and 6-edged face distribution of all the Voronoi polyhedra,

340 where the 5-edged faces are the most abundant (43.91%). **d**, The coordination number

341 distributions for type 1, 2 and 3 atoms.

342
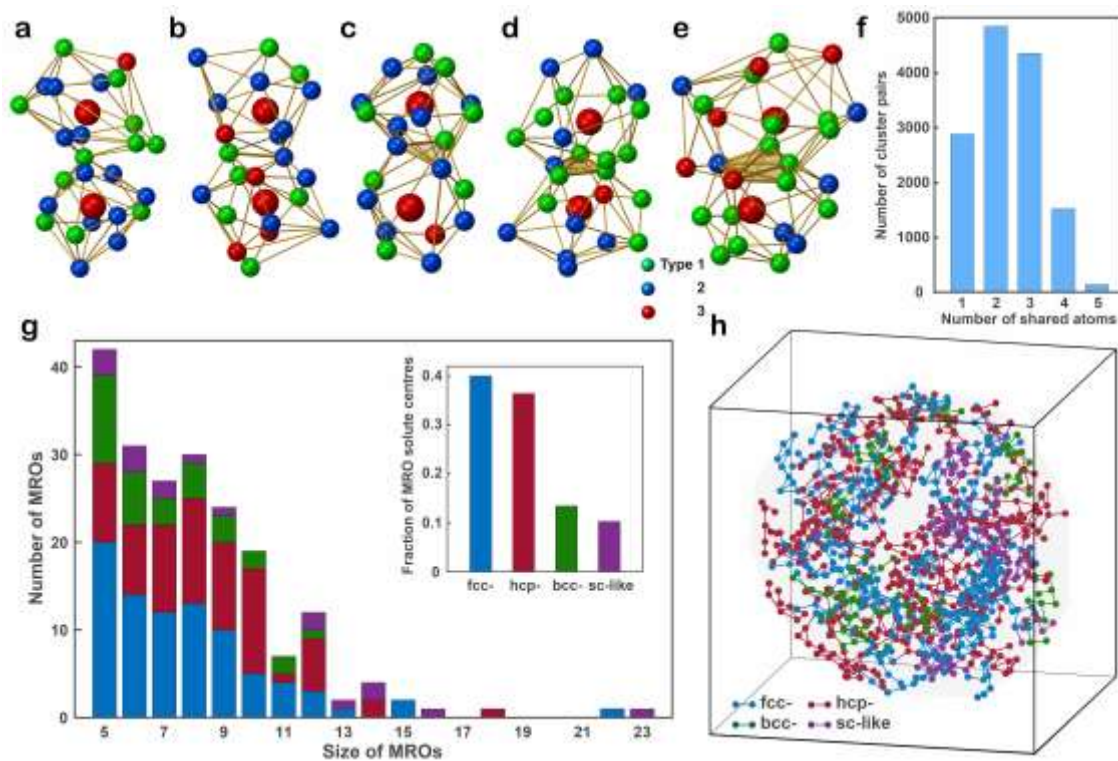
Figure 3 | The connectivity and distribution of the MROs in the glass-forming nanoparticle. **a-e**, Representative pairs of the solute-centred clusters that are connected with each other by sharing one, two, three, four and five atoms, respectively, where the central atom of each cluster is labelled with a large red sphere. **f**, Statistical distribution of the number of the solute-centred cluster pairs, which share from one to five atoms. **g**, Histogram of the four types of MROs – fcc- (in blue), hcp- (in red), bcc- (in green) and sc-like (in purple) – as a function of the size (i.e. the number of solute centres). The total number of fcc-, hcp-, bcc- and sc-like MROs is 85, 71, 31 and 17, respectively. The inset shows the fraction of the solute centre atoms in the four types of MROs. **h**, Distribution of the four types of MROs with eight solute centre atoms or more, where the centre region lacks of large MROs.

354
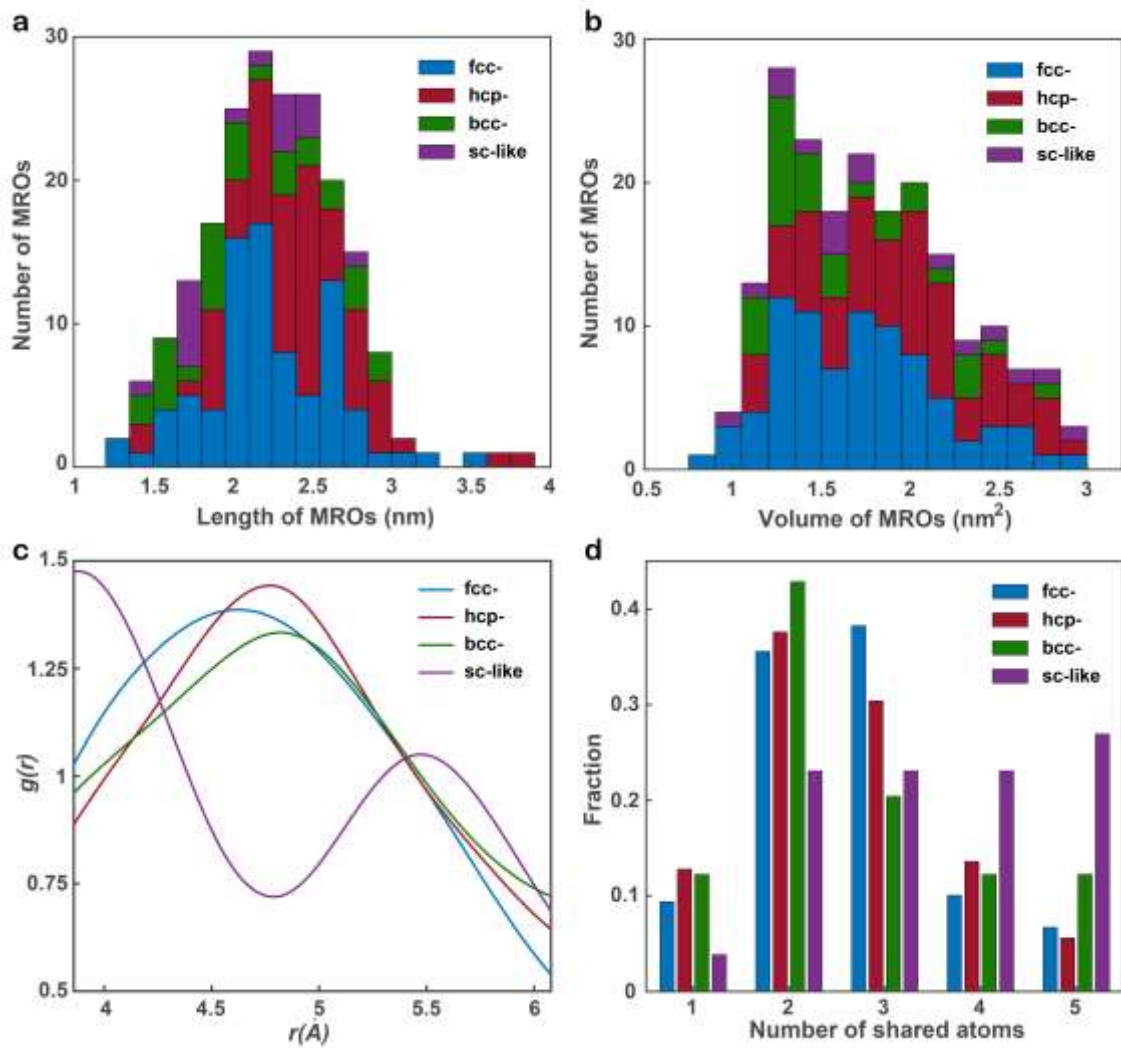
Figure 4 | Quantitative characterization of MROs. The length (**a**) and volume (**b**) distribution of the four types of MROs in the glass-forming nanoparticle, where the length was measured along the longest direction of each MRO. **c,** Partial PDFs of the fcc-, hcp-, bcc- and sc-like solute centres in the glass-forming nanoparticle, where the maximum peak positions are located at 4.62, 4.77, 4.82 and 3.88 Å, respectively. Compared with the other three partial PDFs, the partial PDF of the sc-like solute centres (the purple curve) shows two peaks with the ratio of the second to the first peak position about $\sqrt{2}$. **d,** Distribution of sharing one, two, three, four and five atoms between neighbouring solute-centred clusters for the four types of MROs.
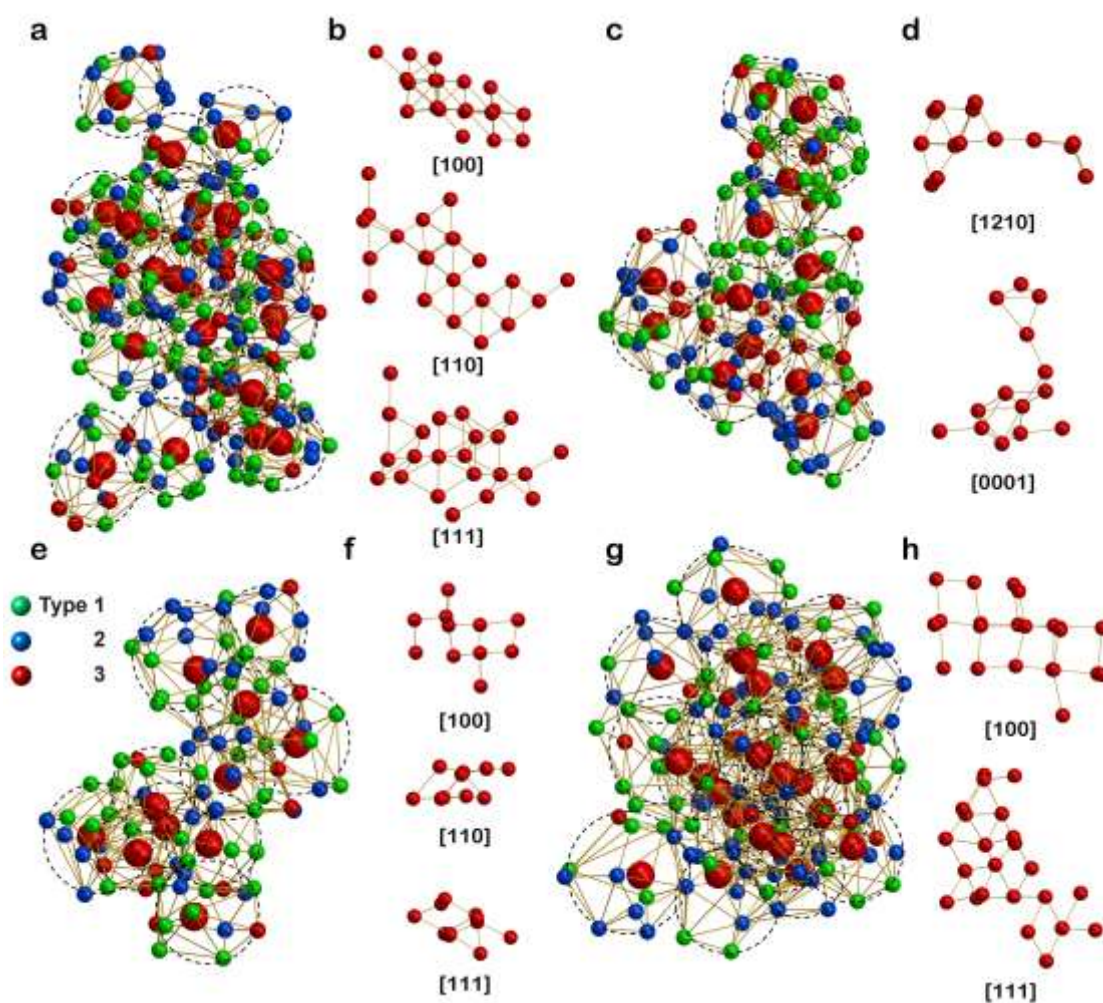
Figure 5 | 3D atomic packing of four representative MROs. Representative fcc- (**a**), hcp- (**c**), bcc- (**e**) and sc-like (**g**) MROs, consisting of 22, 14, 11 and 23 solute centres (large red spheres), respectively, where the individual solute-centred clusters (dashed circles) are randomly oriented. To better visualize the crystal-like MROs, the solvent atoms are removed and the solute centres are orientated along the fcc (**b**), hcp (**d**), bcc (**f**) and sc (**h**) zone axes, showing that the MROs have anisotropic 3D shapes and are severely deviate from the crystal lattices.

METHODS

Sample preparation. The multi-component metallic nanoparticle samples were synthesized using the thermal shock procedures published elsewhere[43]. Individual metal salts (chlorides or their hydrate forms)

375 were dissolved in ethanol at a concentration of 0.05 mol/L. After complete dissolving with hydrochloric

376 acid, the individual salt precursor solutions with different cations were mixed and sonicated for 30 minutes.

377 The homogenously mixed precursor solution was loaded onto the carbon substrates[51] (reduced graphene

378 oxide) and heated to a temperature as high as 1,763 K for 55 milliseconds (Extended Data Fig. 1a). The

379 sample was suspended on a trench and connected with copper electrodes by silver paste for both heating

380 and effective cooling as a giant heat sink. The thermal shock synthesis was triggered by electric Joule

381 heating in an argon-filled glovebox using a Keithley 2425 SourceMeter where the high temperature and

382 duration can be effectively controlled by tuning the input power and duration. The temperature of this

383 process was monitored by a high-speed Phantom Miro M110 camera with a pixel size of 25 μm

384 (Supplementary Video 1). The cooling rate was estimated to be ~5.1-6.9×10^4 K/s (Extended Data Fig. 1a),

385 which, according to previous studies, can make metallic glasses[52,53]. The resulting nanoparticles on reduced

386 graphene oxide were dispersed in ethanol with sonication. After deposited on to 5-nm-thick silicon nitride

387 membranes, the nanoparticles were baked at 100 °C for 12 hours in vacuum to eliminate any hydrocarbon

388 contamination. Both energy-dispersive X-ray and electron energy loss spectroscopy data show that the

389 nanoparticles were still in metallic form and were not oxidized during the experiment (Extended Data Fig.

390 1b-q).

391 **Data acquisition.** A set of tomographic tilt series were acquired from seven nanoparticles using the TEAM

392 0.5 microscope with the TEAM stage[54]. Images were collected at 200 kV in ADF-STEM mode (Extended

393 Data Table 1). To minimize sample drift, four sequential images per tilt angle were measured with a dwell

394 time of 3 μs. To monitor any potential damage induced by the electron beam, we took 0° images before,

395 during and after the acquisition of each tilt series and ensured that no noticeable structural change was

396 observed for the seven nanoparticles. The total electron dose of each tilt series was estimated to be between

397 7×10^5 e$^-$/Å^2 and 9.5×10^5 e$^-$/Å^2 (Extended Data Table 1).

398 **Image pre-processing and denoising.** For each experimental tilt series, we performed the following

399 procedure for image post-processing and denoising.

400 i) Image registration. At each tilt angle, we used the first image as a reference and calculated normalized

401 cross-correlation between the reference and the other three images using a step size of 0.1 pixel[55]. These

402 four images were aligned and summed to form an experimental image at that tilt angle.

403 ii) Scan distortion correction[38]. Two steps were used to correct the scan distortion for the experimental

404 images. First, a set of low-magnification images were taken from nanoparticles and their positions were

405 fitted with a Gaussian. Based on the geometric relation of the nanoparticles at different angles, the scan coil

406 directions were calibrated to be perpendicular and equal in strength. Second, six high-magnification images

407 were taken from a multi-component metallic nanoparticle and scan distortion parameters were estimated

408 by minimizing the mean squared error of the common line of the six images. These scan distortion

409 parameters were applied to the experimental images.

410 iii) Image denoising. The experimental images contain mixed Poisson and Gaussian noise and were

411 denoised by the block-matching and 3D filtering (BM3D) algorithm[56], which has been demonstrated to be

412 effective in reducing noise in AET[38,40,42]. The BM3D denoising parameters were optimized by the following

413 three steps. First, Poisson and Gaussian noise level were estimated from the experimental tilt series. Second,

414 several images were simulated based on a model nanoparticle, which has a similar size and elemental

415 distribution as those of an experimental image. The same level of Poisson and Gaussian noise was added

416 to the simulated images. Third, these noisy images were denoised by BM3D with different parameters. The

417 denoising parameters corresponding to the largest cross-correlation coefficient between the denoised and

418 the original images were chosen and applied to denoise the experimental images.

419 iv) Background subtraction and alignment. After denoising, a 2D mask was defined from each experimental

420 image, which is slightly larger than the size of the nanoparticle. The background inside the mask was

421 estimated by the discrete Laplacian in Matlab. After background subtraction, the experimental images of

422 each tilt series were projected onto the tilt axis to produce a set of 1D curves (termed common lines). The

423 images were aligned along the tilt axis by maximizing the cross-correlation between the common lines. The

424 alignment of the images perpendicular to the tilt axis was achieved by the centre of mass method. The

425 centres of mass of the images were calculated and the images were shifted so that all the centres of mass

426 coincide with the origin. This image alignment method has been successfully used to achieve sub-pixel

427 accuracy[34,36,40-42]. The Matlab data of the raw, processed and aligned experimental images are provided in

428 Supplementary Information.

429 **The REal Space Iterative REconstruction (RESIRE) algorithm.** After post-processing and denoising,

430 the experimental images were reconstructed by the RESIRE algorithm. The algorithm iteratively minimizes

431 an error function defined by,

432
$$\varepsilon_\theta(O) = \frac{1}{2} \sum_{x,y} |\Pi_\theta(O)\{x,y\} - b_\theta\{x,y\}|^2 \qquad (1)$$

433 where $\varepsilon_\theta(O)$ is an error function of a 3D object (O) at tilt angle θ, $\Pi_\theta(O)$ projects O to generate a 2D image

434 at angle θ, b_θ is the experimental image at angle θ, and $\{x,y\}$ is the coordinates. The minimization is

435 solved via the gradient descent,

436
$$\nabla \varepsilon_\theta(O)\{u,v,w\} = \Pi_\theta(O)\{x,y\} - b_\theta\{x,y\} \quad where \begin{bmatrix} u \\ v \\ w \end{bmatrix} = R_\theta \begin{bmatrix} x \\ y \\ z \end{bmatrix} \ for \ some \ z \quad (2)$$

437 where ∇ represents the gradient and R_θ is the rotation matrix at tilt angle θ, which transforms coordinates

438 $\{x,y,z\}$ to $\{u,v,w\}$. The jth iteration of the RESIRE algorithm consists of the following four steps.

439 i) A set of images are calculated from the 3D object of the jth iteration using a Fourier method. The 3D

440 object is first padded with zeros by properly choosing an oversampling ratio[57]. Applying the fast Fourier

441 transform to the zero-padded object generates a 3D array in reciprocal space, from which a series of 2D

442 Fourier slices are obtained at different tilt angles. These 2D Fourier slices are inverted to a set of images

443 via the inverse Fourier transform.

444 ii) The error function defined in equation 1 is calculated between the computed and experimental images.

445 iii) The gradient of the error function is computed for every voxel using equation 2.

446 iv) The 3D object of the (j+1)[th] iteration is updated by,

447
$$O^{j+1} = O^j - \frac{\Delta}{nN} \sum_\theta \nabla \varepsilon_\theta(O^j) \qquad (3)$$

448   where Δ is the step size ($\Delta = 2$ was chosen for the reconstruction of our experimental data), n is the number

449   of images and N is the dimension of each image ($N \times N$). $O^{j+1}\{u, v, w\}$ is used as an input for the $(j+1)^{th}$

450   iteration.

451   The convergence of the algorithm is monitored by the R-factor,

452
$$R = \frac{1}{n}\sum_{\theta}\frac{\sum_{x,y}|\Pi_{\theta}(O)\{x,y\} - b_{\theta}\{x,y\}|}{\sum_{x,y}|b_{\theta}\{x,y\}|} \quad . \quad (4)$$

453   Usually, after several hundreds of iterations, the algorithm converges to a high-quality 3D reconstruction

454   from a limited number of images. Both our numerical simulation and experimental results have indicated

455   that RESIRE outperforms other iterative tomographic algorithms such as generalized Fourier iterative

456   reconstruction[58] and simultaneous iterative reconstruction technique[59]. By avoiding iterating between real

457   and reciprocal space, RESIRE can be applied to general sample geometry such as thin films and extended

458   objects. The details of the RESIRE algorithm will be reported in a follow-up paper.

459   For each aligned experimental tilt series, we first ran RESIRE for 200 iterations. From the initial

460   3D reconstruction, we performed the angular refinement and spatial alignment for the experimental

461   images[40,58]. For each experimental image, we determined the corresponding three Euler angles of the 3D

462   reconstruction. We sequentially scanned each of the three Euler angles with a small angular increment. At

463   each scanning step, we projected the 3D reconstruction back to calculate an image. The experimental image

464   was shifted along the x and y-axis and aligned with the calculated one. An error metric, defined as the

465   difference between the calculated and experimental image, was computed. After scanning all the three Euler

466   angles, three optimal Euler angles was found with the smallest error metric. This procedure was iterated for

467   all the experimental images until there was not further improvement, producing a set of spatially aligned

468   experimental images and refined tilt angles. Next, the background of each experimental image was re-

469   evaluated and re-subtracted. Using these experimental images with the refined tilt angles (Extended Data

470   Fig. 4a), we ran another 200 iterations of RESIRE to obtain the final 3D reconstruction of each experimental

471   tilt series (Extended Data Table 1). The source codes of RESIRE are provided in Supplementary

472   Information.

473   **Determination of 3D atomic coordinates and species.** From each final 3D reconstruction, the atomic

474   coordinates and species were identified using the following procedure[40,42].

475   i) Each 3D reconstruction was upsampled by a factor of 3 using the spline interpolation, from which all the

476   local maxima were identified. Starting from the highest intensity peak, polynomial fitting[60] was performed

477   on a $0.8 \times 0.8 \times 0.8$ Å^3 ($7 \times 7 \times 7$ voxel) volume around each local maximum to locate the peak position. If the

478   distance between the fitted peak position and existing potential atom positions is larger than or equal to 2

479   Å, it was listed as a potential atom. After repeating this step for all the local maxima, a list of potential atom

480   positions was obtained. This method to trace the positions of potential atoms has previously been rigorously

481   tested by using two independent experimental tilt series acquired from the same sample[42].

482   ii) A 3D difference map was generated by taking the difference between the 3D reconstruction and the list

483   of the potential atoms. Based on the difference map, we manually adjusted a very small fraction of the

484   atoms (167 out of 18356), which has been routinely used in protein crystallography[61].

485   iii) A K-mean clustering method[40,42,62] was used to classify three types of atoms and non-atoms (Co and Ni

486   as type 1, Ru, Rh, Pd and Ag as type 2, and Ir and Pt as type 3) based on the integrated intensity of a 0.8 Å

487     $\times$ 0.8 Å $\times$ 0.8 Å volume around each potential atom position. An initial atomic model with 3D atomic

488   coordinates was determined from each 3D reconstruction.

489   iv) Due to the missing wedge problem and noise in the experimental images, there is local intensity

490   variation in each 3D reconstruction. A local reclassification was iteratively performed to refine the type 1,

491   2 and 3 atoms. Each atom was defined as the centre of a 10-Å-radius sphere. The average intensity

492   distribution of type 1, 2 and 3 atoms was computed within the sphere. The L_2 norm of the intensity

493   distribution between the centre atom and the average type 1, 2 and 3 atom was calculated. The centre atom

494   was assigned to the type with the smallest L_2 norm. The procedure was iteratively repeated until there were

495   no further changes. The source codes for 3D atom tracing and classification are provided in Supplementary

496   Information.

497   **Refinement of 3D atomic coordinates.** The 3D atomic coordinates were refined by minimizing the error

498   between the calculated and measured images using the gradient descent[38,40,42]. Each atom was first fit with

499   a 3D Gaussian function with a height H and a width B', where H and B' were considered the same for the

500   same type of atoms. A 3D atomic model was obtained by,

501
$$O\{x,y,z\} = \sum_i H_i \exp\left[-\frac{|x-x_i|^2 + |y-y_i|^2 + |z-z_i|^2}{B_i'}\right] \quad (5)$$

502   where x_i, y_i, z_i, H_i and B_i' are the coordinates, height and standard deviation of the ith atom, respectively,

503     $|x-x_i|, |y-y_i|, |z-z_i| \le \rho$, and ρ is a cut-off size of the 3D Gaussian function. From the 3D atomic

504   model, a set of projection images were computed at different tilt angle θ by,

505
$$\Pi_\theta(O)\{u,v\} = \sum_w \sum_i H_i \exp\left[-\frac{|u-u_i|^2 + |v-v_i|^2 + |w-w_i|^2}{B_i'}\right] \quad (6)$$

506
$$\text{where } \begin{bmatrix} u_i \\ v_i \\ w_i \end{bmatrix} = R_\theta \begin{bmatrix} x_i \\ y_i \\ z_i \end{bmatrix} \quad and \quad |u-u_i|, |v-v_i|, |w-w_i| \le \rho.$$

507   Substituting equation (6) into (1), an error function was calculated, from which the gradient descent method

508   was used to search for the optimal atomic position at the $(j+1)^{th}$ iteration,

509
$$\{x_i, y_i, z_i\}^{j+1} = \{x_i, y_i, z_i\}^j - \Delta \sum_\theta [\Pi_\theta(O)\{u,v\} - b_\theta\{u,v\}]\nabla_i[\Pi_\theta(O)\{u,v\}] \quad (7)$$

510   Where ∇_i is the spatial gradient operator with respect to the atomic position (x_i, y_i, z_i). The iterative

511   refinement process was terminated when the L_2 norm error could not be further reduced.

512   **3D precision estimation with multislice simulations**. A tilt series of 55 STEM images were calculated

513   from the experimental 3D atomic model by using a fast multislice simulation software based on graphics

514   processing unit[66]. At each refined experimental angle (Extended Data Fig. 4a), the experimental 3D atomic

515   model was placed in a cuboidal super cell and the super cell was divided into multiple 2-Å-thick slices

516   along the z-axis. The experiment parameters shown in Extended Data Table 1 (particle 1) were used for the

517   multislice simulations. After using the parallel computing to perform the multislice simulations for all the

518   angles, we calculated 55 multislice STEM images, each with 289$\times$289 pixels and a pixel size of 0.347 Å.

519   To account for the electron probe size and other incoherent effects, each multislice STEM image was

520   convolved with a Gaussian kernel. Extended Data Fig. 4c and d show a representative experimental and

521   multislice STEM image, respectively. An average R-factor between the 55 experimental and multislice

522   images (defined in equation 4) was computed to be 14.96%, which, according to the crystallography

523   standard[61], represents a good agreement between the two sets of images.

524   From the 55 multislice STEM images with angular errors (Extended Data Fig. 4a), we performed

525   the 3D reconstruction and angular refinement with RESIRE (Extended Data Fig. 4b). After applying the

526   atomic tracing, classification and refinement procedure to the reconstruction, we obtained a new 3D atomic

527   model of the sample, consisting of 8438, 6905 and 3138 type 1, 2, and 3 atoms, respectively. We identified

528   7898, 6837, 3138 common pairs of type 1, 2 and 3 atoms, respectively, between the experimental and

529   multislice atomic models based on the criterion of each common pair within a radius of 1.5 Å. The total

530   common pairs of the three types of atoms are 17873, indicating that 97.37% of all atoms have been corrected

531   identified. Extended Data Fig. 4d shows the distribution of the atomic deviation between all the common

532   pairs with the root-mean-square deviation (i.e. 3D precision) of 21 pm.

533   **The local bond orientational order (BOO) parameters**. The local BOO parameters (Q_4 and Q_6) were

534   calculated from the 3D atomic model of each nanoparticle using a method described elsewhere[63,64]. The Q_4

535   and Q_6 order parameters were computed up to the second shell with a shell radius set by the first valley in

536   the PDF curve of the 3D atomic model. Figure 1f and Extended Data Fig. 2h-n show the distribution of the

537   local BOO parameters of all the atoms in particles 1-7. To separate the amorphous structure from the crystal

538   nuclei, we calculated the normalized BOO parameter, defined as $\sqrt{Q_4{}^2 + Q_6{}^2}/\sqrt{Q_{4\,\mathrm{fcc}}^2 + Q_{6\,\mathrm{fcc}}^2}$, where

539      $Q_{4\,\mathrm{fcc}}$ and $Q_{6\,\mathrm{fcc}}$ are the Q_4 and Q_6 value for a perfect fcc lattice. The normalized BOO parameter is between

540   0 and 1, where 0 means $Q_4 = Q_6 = 0$ and 1 represents a perfect fcc crystal structure. Based on the BOO

541   parameters of a $Cu_{65}Zr_{35}$ metallic glass structure obtained from molecular dynamics simulations[65]

542   (Extended Data Fig. 2o), we chose the normalized BOO parameter = 0.5 as a cut-off to separate crystal

543   nuclei from amorphous structure (red curves in Fig. 1f and Extended Data Fig. 2h-n).

544   **Characterization of the crystalline-amorphous interface**. The 3D surface of each crystal nucleus was

545   defined by setting the normalized BOO parameter ≥ 0.5. For every atom, the perpendicular distance to the

546   3D surface of its closest crystal nucleus was calculated. If the atom is inside the nucleus, the distance is

547   negative, otherwise it is positive. After counting all the atoms in the nanoparticle, a 1D curve was created

548   to represent the normalized BOO parameter as a function of the distance. An exponential decay function

549      $y = ae^{-x/d_c} + b$ was used to fit the 1D curve, where a and b are two constant, and d_c is the characteristic

550   width of the crystalline-amorphous interface. For the crystal nuclei in the glass-forming nanoparticle, d_c

551   was determined to be 3.69 Å, which is consistent with the molecular dynamics simulation of a poor glass

552   former[30].

553   **PDF and partial PDF.** The PDF was calculated for the 3D atomic model of each nanoparticle using the

554   following procedure. i) The distance of all atom pairs in each 3D atomic model was computed and binned

555   into a histogram. ii) The number of atom pairs in each bin was normalized with respect to the volume of

556   the spherical shell corresponding to each bin. iii) The histogram was scaled so that the PDF approaches one

557 for large separations. After plotting the PDF for each nanoparticle, the first valley of the PDF was used as

558 the nearest neighbour cut-off distance to calculate the local BOO parameters (Fig. 1f and Extended Data

559 Fig. 2h-n). By choosing the atoms in the glass-forming nanoparticle (particle 1) with the normalized BOO

560 parameter < 0.5, we applied the above procedure to plot the PDF (Fig. 1g). For type 1, 2 and 3 atoms, we

561 identified six sets of atoms pairs (type 11, 12, 13, 22, 23 and 33) in the nanoparticle. For each set of atom

562 pairs, we used the above procedure to calculate the partial PDF shown in Fig. 1h.

563 **Voronoi tessellation and the coordination number (CN).** The analysis of the Voronoi tessellation was

564 performed by following the procedure published elsewhere[6], where the surface atoms of the nanoparticle

565 were excluded. To reduce the effect of the experimental and reconstruction error on Voronoi tessellation,

566 those surfaces with areas less than 1% of the total surface area of each Voronoi polyhedron were removed[9].

567 From the Voronoi tessellation, each polyhedron is designated by a Voronoi index $\langle n_1, n_2, n_3, n_4, \cdots \rangle$ with

568 n_i denoting the number of i-edged faces and the CN was calculated by $\sum_i n_i$.

569 To examine the effect of the 3D precision of AET on the Voronoi tessellation, we used a $Cu_{65}Zr_{35}$

570 metallic glass structure obtained from molecular dynamics simulations[65]. A 3D atomic model was cropped

571 from the structure to have the similar 3D shape and size to the experimental nanoparticle (particle 1). Our

572 Voronoi analysis reveals that the ten most abundant Voronoi polyhedra in the atomic model are <0,0,12,0>,

573 <0,2,8,2>, <0,2,8,1>, <0,1,10,2>, <0,3,6,4>, <0,3,6,3>, <0,1,10,4>, <0,2,8,4>, <0,1,10,3> and <0,0,12,3>.

574 Their corresponding fractions are 14.26%, 10.26%, 7.97%, 6.92, 4.58%, 4.14%, 4.01%, 3.41%, 2.97% and

575 2.32%, respectively. After adding the experimental error (Extended Data Fig. 4e) to the atomic model, the

576 corresponding fractions of these ten Voronoi polyhedra become 13.70%, 9.95%, 7.91%, 6.97%, 4.63%,

577 4.08%, 3.57%, 3.42%, 2.89% and 2.19%, respectively. This analysis indicates that the 3D precision of AET

578 has only a small effect on the Voronoi tessellation.

579 **Quantification of the chemical SRO.** We used the Warren–Cowley parameters (α_{lm}) to quantify the

580 chemical SRO[67,68],

581
$$\alpha_{lm} = 1 - \frac{Z_{lm}}{\chi_m Z_l} \qquad (8)$$

582 where $l, m = 1, 2$ or 3, Z_{lm} is the partial CN of type m atoms around type l atoms, χ_m is the fraction of

583 type m atoms, and Z_l is the total CN around type l atoms. After excluding the surface atoms, we estimated

584 χ_1, χ_2 and χ_3 to be 42.97%, 38.28% and 18.75%, respectively. Using the partial CNs (Extended Data Fig.

585 5b), we calculated $\alpha_{11} = -0.11$, $\alpha_{12} = 0.1$, $\alpha_{13} = 0.05$, $\alpha_{21} = 0.02$, $\alpha_{22} = 0.01$, $\alpha_{23} = -0.07$, $\alpha_{31} = 0.03$, α_{32}

586 $= -0.06$, and $\alpha_{33} = 0.06$, indicating that the type 11 and 23 bonds are favoured, but the type 12 and 33 bonds

587 are unfavoured. These results are consistent with the observations that the type 23 bond is 0.06 Å shorter

588 than the average type 2 and 3 bonds and the type 12 bond is 0.06 Å longer than the average type 1 and 2

589 bonds (Fig. 1h).

590 **Determination of the solute centres and MROs.** A breadth-first-search algorithm[69,70] was implemented

591 to search for the solute centres and MROs using the following procedure. First, the algorithm identified the

592 solute centres from type 3 atoms based on two criteria: i) each solute centre must fall within a 0.75 Å radius

593 from an fcc, hcp, bcc or sc lattice point; and ii) each solute centre must have at least one neighbouring type

594 3 atom within the second-coordination-shell distance. Second, the identified solute centres were sorted out

595   to generate a queue of the fcc-, hcp-, bcc- or sc-like MRO candidates. Third, starting from the largest MRO

596   candidate (i.e. with the most solute centres), each candidate was classified as an MRO if it has at least five

597   or more solute centres and none of the solute centres was already occupied by another MRO. If any solute

598   centres were already occupied, they were removed from the MRO candidate and the candidate was refitted

599   into the lattice vectors and added back into the queue. If two or more MRO candidates have the same

600   number of solute centres, the one with the smallest error of fitting the solute centres into the lattice vectors

601   was analysed first. This process was repeated until all the MROs were identified, where each solute centre

602   can only belong to no more than one MRO. To corroborate our analysis, we repeated the above steps with

603   a 1 Å and 0.5 Å radius cut-off and the corresponding MROs are shown in Extended Data Figs. 6 and 7,

604   respectively.

605   An attempt was also made in searching for icosahedral-like MROs. The breadth-first-search

606   algorithm[69,70] was used to find the MROs that falls within a 0.75 Å radius from the 12 vertices of an

607   icosahedron. Because the icosahedron cannot be periodically packed in three dimensions, only the nearest

608   neighbour vertices were searched, making the largest possible MRO have 13 solute centres (1 central solute

609   centre plus 12 nearest neighbours). After performing the search, the resulting possible MROs have a mean

610   value of 3.9, meaning on average each solute centre is connected to only 3 others when constrained to an

611   icosahedron within the second coordination shell. Furthermore, although the largest possible MRO has 7

612   solute centres, none of these solute centres form 5-fold symmetry. We also repeated this analysis with a 1

613   Å radius cut-off. The mean value of solute centres becomes 4.5, the largest MRO has 8 solute centres, and

614   there are 19 5-fold symmetries. The source codes for identifying the MROs are provided in Supplementary

615   Information.

616   **Determination of the 3D atomic structure of an amorphous CuTa thin film**. The following procedure

617   was used to experimentally resolve the 3D atomic positions in the CuTa thin film.

618   i) Sample preparation. CuTa thin films were fabricated *in-situ* in the sample chamber of the spin polarized

619   low energy electron microscope (SPLEEM) at NCEM, where clean ultrahigh vacuum conditions remained

620   in the low 10^{-9} torr range. Using thermal evaporation, CuTa thin films were deposited on Si_3N_4 substrates,

621   which were maintained well below 150 K during sample fabrication. The growth rate of the thin films was

622   in the range of 0.1 – 1 atomic monolayer per minute. After the fabrication of the CuTa thin films, a very

623   thin carbon capping layer was deposited on the films to protect the samples from oxidation.

624   ii) Data acquisition. A tomographic tilt series was acquired from the CuTa thin film using TEAM I under

625   ADF-STEM mode at 300 kV. To mitigate the sample drift, two images at each tilt angle were taken and

626   then aligned to improve the signal-to-noise ratio. The tilt series consists of a total of 40 images with a tilt

627   range from -67.9° to 64.9° (Extended Data Fig. 8). As the CuTa film is thinner than ~6 nm, 40 experimental

628   images are sufficient to produce a good 3D reconstruction. The total electron dose of the dataset is 4.8×10^5

629     $e/Å^2$. All the experimental parameters of the tilt series can be found in Extended Data Table 1.

630   iii) Image alignment. All the image pre-processing and denoising steps for the analysis of the CuTa thin

631   film are similar to those of the glass-forming nanoparticle, except for image alignment. We first used the

632   cross-correlation between the neighbouring images to roughly align the CuTa images. Next, we searched

633   for some reference markers, which can be either created by adding some small nanoparticles or based on

634   features in the sample. In this experiment, we chose an isolated region in the images and aligned them using

635   the centre of mass and common line method[34,36]. After obtaining the 3D reconstruction, we further refined

636   the alignment by projecting the reconstruction back to generate images and comparing them with the

637   experimental ones. This process was repeated until no further improvement could be made.

638   iv) 3D reconstruction, atomic tracing and refinement. Using RESIRE, we first performed a large volume

639   reconstruction of the CuTa thin film from the aligned images. Based on the thickness variation of the thin

640   film, we applied scanning AET[41] to conduct multiple local volume reconstructions and then patched them

641   together to produce a full 3D reconstruction. Scanning AET has been previously demonstrated to be

642   effective in improving the 3D reconstruction of 2D materials and/or thin film samples[41]. From the full 3D

643   reconstruction, we projected it back to generate images and use them to perform the angular refinement and

644   spatial alignment. We iteratively repeated the process until there were no further changes. After obtaining

645   the final 3D reconstruction, we traced the Cu and Ta atoms based on the integrated intensity difference

646   between the two types of atoms. The 3D atomic positions were refined to produce a final 3D atomic model

647   of the CuTa thin film (Extended Data Fig. 9).

648

Data availability

650   The raw and processed experimental data can be freely downloaded at https://github.com/AET-

651   MetallicGlass/Supplementary-Data-Codes. The 3D atomic coordinates of the glass-forming nanoparticle

652   has been deposited in the Materials Data Bank (MDB, www.materialsdatabank.org) with the MDB ID:

653   NiRh00001.

Code availability

655   All the MATLAB source codes for the RESIRE reconstruction and data analysis of this work are freely

656   available at https://github.com/AET-MetallicGlass/Supplementary-Data-Codes.

657   51. Xu, Z., Sun, H., Zhao, X. & Gao, C. Ultrastrong fibers assembled from giant graphene oxide
658   sheets. *Adv. Mater.* **25**, 188-193 (2013).

659   52. Takeuchi, A. & Inoue, A. Quantitative evaluation of critical cooling rate for metallic glasses.
660   *Mater. Sci. Eng.* A **304-306**, 446–451 (2001).

661   53. Bordeenithikasem, P. et al. Determination of critical cooling rates in metallic glass forming alloy
662   libraries through laser spike annealing. *Sci Rep* **7**, 7155 (2017).

663   54. Ercius, P., Boese, M., Duden, T. & Dahmen, U. Operation of TEAM I in a user environment at
664   NCEM. *Microsc. Microanal.* **18**, 676-683 (2012).

665   55. Lewis, J. P. Fast normalized cross-correlation. *Vis. Interface* **95**, 120-123 (1995).

666   56. Dabov, K., Foi, A., Katkovnik, V. & Egiazarian, K. Image denoising by sparse 3-D transform-
667   domain collaborative filtering. *IEEE Trans. Image Process.* **16**, 2080-2095 (2007).

668   57. Miao, J., Sayre, D. & Chapman, H. N. Phase retrieval from the magnitude of the Fourier transform
669   of non-periodic objects, *J. Opt. Soc. Am. A* **15**, 1662-1669 (1998).

58. Pryor, A. et al. GENFIRE: a generalized Fourier iterative reconstruction algorithm for high-resolution 3D imaging. *Sci. Rep.* **7**, 10409 (2017).

59. Gilbert, P. Iterative methods for the three-dimensional reconstruction of an object from projections. *J. Theor. Biol.* **36**, 105-117 (1972).

60. Rogers, S. S., Waigh, T. A., Zhao, X. & Lu, J. R. Precise particle tracking against a complicated background: polynomial fitting with Gaussian weight. *Phys. Biol.* **4**, 220–227 (2007).

61. Brünger, A. T. et al. Crystallography & NMR System: a new software suite for macromolecular structure determination. *Acta Crystallogr. D* **54**, 905–921 (1998).

62. Lloyd, S. Least squares quantization in PCM. *IEEE Trans. Infor. Theory* **28**, 129-137 (1982).

63. Steinhardt, P. J., Nelson, D. R. & Ronchetti, M. Bond-orientational order in liquids and glasses. *Phys. Rev. B* **28**, 784-805 (1983).

64. Lechner, W. & Dellago, C. Accurate determination of crystal structures based on averaged local bond order parameters. *J. Chem. Phys.* **129**, 114707 (2008).

65. Yu, H. B. & Samwer, K. Atomic mechanism of internal friction in a model metallic glass. *Phys. Rev. B* **90**, 144201 (2014).

66. Pryor, A., Ophus, C. & Miao, J. A streaming multi-GPU implementation of image simulation algorithms for scanning transmission electron microscopy. *Adv. Struct. Chem. Imag.* **3**, 15 (2017).

67. Warren, B. E. *X-ray diffraction* (New York: Dover Publications Inc. 1990).

68. Cowley, J. M. X-Ray Measurement of order in single crystals of Cu_3Au. *J. Appl. Phys.* **21**, 24-29 (1950).

69. Lee, C. Y. An algorithm for path connections and its applications. *IEEE Trans. Electron. Comput.* **EC-10**, 346-365 (1961).

70. Larsen, P. M., Schmidt, S. & Schiøtz, J. Robust structural identification via polyhedral template matching. *Model. Simul. Mater. Sci. Eng.* **24**, 055007 (2016).

719

720 **Extended Data legends**

721

722 **Extended Data Fig. 1 | Cooling rate measurement, energy-dispersive X-ray (EDX)**

723 **and electron energy loss spectroscopy (EELS) maps of the nanoparticles**. **a,** The

724 cooling rate for the average and maximum temperature curves was measured to be 51000

725 K/s (the slope of the red line) and 69000 K/s (the slope of the green line), respectively. **b,**

726 Low-resolution ADF-STEM image of the nanoparticles. EDX maps show the distribution

727 of Ni (**c**), Co (**d**), Ru (**e**), Rh (**f**), Pd (**g**), Ag (**h**), Ir (**i**) and Pt (**j**). **k,** The EDX spectrum of

728 all the elements shown in the images (**c-j**), where cps stands for counts per second. **l,**

729 Low-resolution ADF-STEM image of a large area, in which the white square indicates

730 the aggregation of several nanoparticles used for the EELS measurement. **m,** ADF-STEM

731 image of the white square region. **n**–**p,** EELS maps show the distribution of Co (**n**), Ni

732   (**o**) and O (**p**) in the region. **q**, EELS spectrum obtained from (**n**–**p**). No oxygen signal

733   was detected in the EELS map or spectrum. Scale bars, 20 nm in (**b**), 100 nm in (**l**) and

734   10 nm in (**o**).

735

736   **Extended Data Fig. 2 | Analysis of seven multi-component metallic nanoparticles. a-**

737   **g**, Representative ADF-STEM images of particles 1-7, respectively. Scale bar, 2 nm. **h-**

738   **n**, Local BOO parameters of all the atoms in particles 1-7, where the dashed red curves

739   correspond to the normalized BOO parameter = 0.5. The percentage on the top of each

740   panel shows the fraction of disordered atoms in each particle. **o**, Local BOO parameters

741   of a 3D atomic model cropped from a molecular dynamics simulated $Cu_{65}Zr_{35}$ metallic

742   glass[65] as a reference, from which the normalized BOO parameter = 0.5 (dashed red

743   curve) was chosen as a cut-off to separate crystal nuclei from amorphous structure. For a

744   fair comparison, the 3D atomic model was cropped to have the similar 3D shape and size

745   to the experimental nanoparticle (particle 1). **p-v**, PDFs of all the atoms in particles 1-7,

746   respectively. With the decrease of the fraction of disordered atoms in the nanoparticles,

747   the peaks in the PDFs become narrower and new peaks corresponding to different crystal

748   planes appear.

749

750   **Extended Data Fig. 3 | Experimental tomographic tilt series of the multi-component**

751   **glass-forming nanoparticle (particle 1).** 55 raw ADF-STEM images of the nanoparticle

752   with a tilt range from -69.4° to +72.6°. The power spectra of the images are shown in the

753   insets, where the amorphous halo is visible. Some crystalline features are visible in

754   several experimental images and the 2D power spectra. Scale bar, 2 nm.

755

756 **Extended Data Fig. 4 | Angular errors in the experimental images and verification**

757 **of the experimental 3D atomic model using multislice simulations. a**, Angular errors

758 in the experimental images determined by the angular refinement procedure (Methods),

759 where the colour dots and lines represent the deviation of the three Euler angles $(\phi, \theta$ and

760 $\varphi)$ from the correct ones $(0°)$ at each tilt angle. These angular errors were taken into

761 account in the multislice simulations. **b**, The angular errors were correctly refined in the

762 3D reconstruction of the 55 multislice images using RESIRE (Methods). After the angular

763 refinement, the largest error is only $0.2°$. Comparison between a representative

764 experimental (after denoising) (**c**) and a multislice image (**d**) at $0°$. To account for the

765 source size and incoherent effects, each multislice image was convolved with a Gaussian

766 function (Methods). **e**, Histogram of the deviation of the atomic positions between the

767 experimental atomic model and that obtained from 55 multislice images. The peak, mean

768 and root-mean-square deviation of the histogram are 6 nm, 15 nm and 21 pm,

769 respectively. Scale bar, 2 nm.

770

771 **Extended Data Fig. 5 | 3D distribution of the crystal nuclei in the glass-forming**

772 **nanoparticle, the partial CNs and the Voronoi polyhedra of the solute-centred**

773 **clusters. a**, 3D distribution of the atoms with the normalized BOO parameter ≥ 0.5,

774 revealing 15.46% of the total atoms forming crystal nuclei in the nanoparticle. **b**,

775 Normalized partial CNs of type 1, 2 and 3 atoms. **c**, 3D distribution of the 2682 solute

776 centres (red dots), which are between the first (3.78 Å) and the second minimum (6.09 Å)

777 of the PDF curve (Fig. 1g). **d**, Ten most abundant Voronoi polyhedra of the solute-centred

778 clusters.

779

780   **Extended Data Fig. 6 | Identification of MROs with a 1 Å radius cut-off. a**, Histogram

781   of the four types of MROs − fcc- (in blue), hcp- (in red), bcc- (in green) and sc-like (in

782   purple) − as a function of the size (i.e. the number of solute centres). **b**, The population

783   of the solute centre atoms for the four types of MROs. Representative fcc- (**c**), hcp- (**e**),

784   bcc- (**g**) and sc-like (**i**) MROs, containing 23, 18, 10 and 27 solute centres (large red

785   spheres), respectively. The solute centres are orientated along the fcc (**d**), hcp (**f**), bcc (**h**)

786   and sc (**j**) zone axes.

787

788   **Extended Data Fig. 7 | Identification of MROs with a 0.5 Å radius cut-off. a**,

789   Histogram of the four types of MROs − fcc- (in blue), hcp- (in red), bcc- (in green) and

790   sc-like (in purple) − as a function of the size. **b**, The population of the solute centre atoms

791   for the four types of MROs. Representative fcc- (**c**), hcp- (**e**), bcc- (**g**) and sc-like (**i**)

792   MROs, containing 15, 10, 8 and 8 solute centres (large red spheres), respectively. The

793   solute centres are orientated along the fcc (**d**), hcp (**f**), bcc (**h**) and sc (**j**) zone axes.

794

795   **Extended Data Fig. 8 | Tomographic tilt series of an amorphous CuTa thin film. a**,

796   ADF-STEM images of a portion of the CuTa thin film. The insets show the 2D power

797   spectra of the experimental images, in which the diffuse halos are clearly visible. Scale

798   bar, 2 nm.

799

800   **Extended Data Fig. 9 | Determination of the 3D atomic structure of the amorphous**

801   **CuTa thin film. a**, A large field of view of the amorphous CuTa. **b**, Magnified white

802   square region in (**a**). **c**, Average 2D power spectrum of all the experimental images. **d**,

803   3D atomic model of the portion of the CuTa thin film with a total of 1808 Cu (in gold)

804   and 12774 Ta (in blue) atoms, determined from the tilt series shown in Extended Data

805   Fig. 8a (Methods). As the CuTa film is thinner than ~6 nm, 40 experimental images are

806   sufficient to produce a good 3D reconstruction. **e**, A 2-Å-thick internal slice of the 3D

807   reconstruction of the amorphous CuTa thin film, showing the disordered atomic structure.

808   **f**, Local BOO parameters of the 3D atomic model, where only 0.47% of the total atoms

809   with the normalized BOO parameter ≥ 0.5 form crystal nuclei. **g**, PDF of the disordered

810   atoms with the normalized BOO parameter < 0.5. Scale bars, 30 nm in (**a**), 2 nm in (**b**)

811   and (**e**).

812

813   **Extended Data Table 1 | AET data collection, processing, reconstruction, refinement**

814   **and statistics.** [a]The R_1-factor is defined as equation 5 in ref. 40. [b]The R-factor is defined

815   in equation 4 in Methods.